ACS NANO

www.acsnano.org

ARTICLE

Centimeter-Scale Tellurium Oxide Films for Artificial Optoelectronic Synapses with Broadband Responsiveness and Mechanical Flexibility

Chung Won Lee, Changhyeon Yoo, Sang Sub Han, Yu-Jin Song, Seung Ju Kim, Jung Han Kim, and Yeonwoong Jung*

Cite This: *ACS Nano* 2024, 18, 18635−18649

Read Online

ACCESS | Metrics & More | Article Recommendations | Supporting Information

ABSTRACT: Prevailing over the bottleneck of von Neumann computing has been significant attention due to the inevitableness of proceeding through enormous data volumes in current digital technologies. Inspired by the human brain's operational principle, the artificial synapse of neuromorphic computing has been explored as an emerging solution. Especially, the optoelectronic synapse is of growing interest as vision is an essential source of information in which dealing with optical stimuli is vital. Herein, flexible optoelectronic synaptic devices composed of centimeter-scale tellurium dioxide (TeO_2) films detecting and exhibiting synaptic characteristics to broadband wavelengths are presented. The TeO_2-based flexible devices demonstrate a comprehensive set of emulating basic optoelectronic synaptic characteristics; i.e., excitatory postsynaptic current (EPSC), paired-pulse facilitation (PPF), conversion of short-term to long-term memory, and learning/forgetting. Furthermore, they feature linear and symmetric conductance synaptic weight updates at various wavelengths, which are applicable to broadband neuromorphic computations. Based on this large set of synaptic attributes, a variety of applications such as logistic functions or deep learning and image recognition as well as learning simulations are demonstrated. This work proposes a significant milestone of wafer-scale metal oxide semiconductor-based artificial synapses solely utilizing their optoelectronic features and mechanical flexibility, which is attractive toward scaled-up neuromorphic architectures.

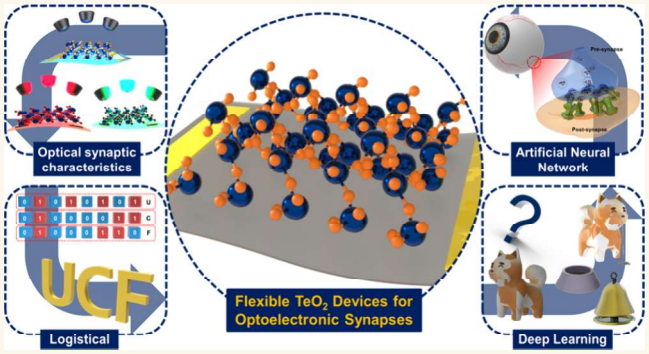

KEYWORDS: *tellurium oxide, photodetector, flexible device, optoelectronic device, optical synapse, neuromorphic computation, artificial neural network*

INTRODUCTION

Conventional digital computing process based on von Neumann architectures is encountering serious challenges in the generation of artificial intelligence (AI) owing to its intrinsic drawbacks, including the physical separation of memory and central processing units which causes excessive energy consumption.[1−5] Accordingly, alternative methods to handle the big data demanded in the AI-driven Internet of Things (IoTs) have been explored, leading to an emergence of the neuromorphic computation, which mimics the operation of human brain synapses. Neuromorphic computing based on artificial synapses offers distinct advantages including high-speed operation and high energy efficiency, as well as proficiency in learning, recognition, and complex calculations.[6−12] Recently, a variety of synaptic devices in diverse configurations such as two-terminal memristors[13,14] and three-terminal transistors[15,16] are proposed, which employ purely electrical stimuli to generate and modulate synaptic weights. However, this electrical input-driven synaptic operation is intrinsically limited to low process rates due to the bandwidth-connection-density trade-off and issues of interconnection.[17,18]

Received: April 12, 2024
Revised: June 17, 2024
Accepted: June 18, 2024
Published: July 1, 2024

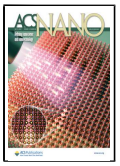

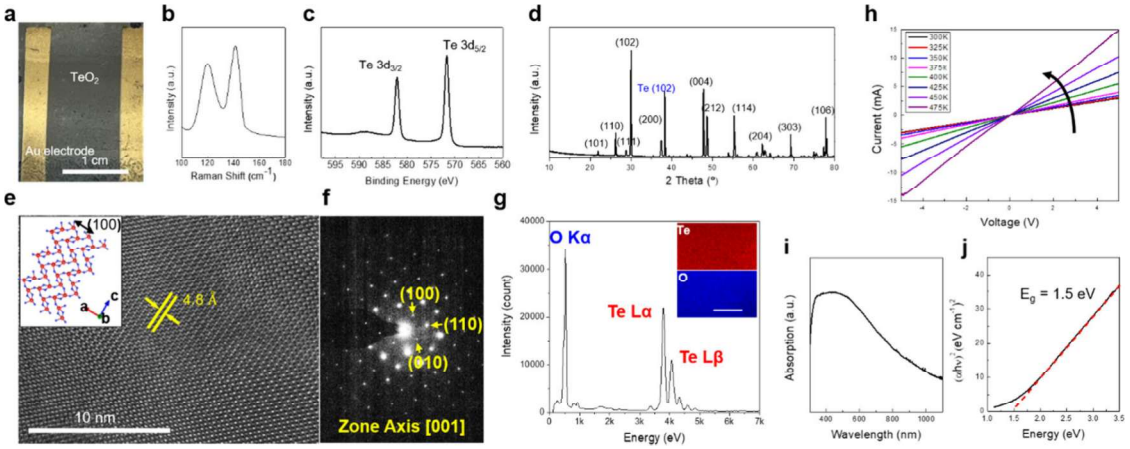

Figure 1. Large-area TeO_2 film growth and structural, chemical, electrical characterizations. (a) Image of centimeter-scaled TeO_2 film grown on Si/SiO_2 substrate with two-terminal Au electrodes. (b) Raman spectrum of TeO_2 film. (c) XPS spectra for Te 3d. (d) XRD profiles of TeO_2 film. (e) Cross-sectional HRTEM of tetragonal TeO_2. (f) SAED patterns of tetragonal TeO_2. (g) EDS spectrum obtained from the sample of (e). The inset shows EDS elemental mapping images where the scale bar is 1 μm. (h) Temperature-dependent $I-V$ characteristics of TeO_2. (i) UV−vis absorbance spectrum of TeO_2. (j) Tauc plot corresponding to (i).

Meanwhile, from the optical synapses' point of view, it is noted that human neural systems involve up to 80% of sensory stimuli from the external atmosphere such as light illumination.[19] In order to take a full advantage of such functional features inherent to the biological systems, a state-of-the-art concept of optoelectronic synaptic devices emerged; i.e., synaptic devices capable of converting optical stimuli to electrical signals and/or replicating visual perception, processing, and memory functions within artificial visual systems.[20−23] In fact, employing optical stimuli in neuromorphic systems promotes the speed of computational calculations with low energy consumptions, crosstalk, and high bandwidth.[18] Also, compared with three-terminal electrically gated synaptic devices,[20,24−28] two-terminal optical systems offer the advantages of simple and low-cost fabrication, similarity to biological neurons, and facile vertical integration.[29,30]

From the device components' point-of-view, metal oxides were conventionally adopted for artificial synapses (i.e., switching media for memristors and channels for transistors)[31−33] due to their low-cost and simple manufacturability coupled with high stability and optical transparency.[34−37] However, they typically possess large energy bandgaps (>3 eV),[38−41] which limits their optical inputs to employing the photons of high energies with short wavelengths near the ultraviolet (UV) spectrum region. Meanwhile, optical operation adopting visible light with a broad range of wavelengths will lead to more efficient photocurrent generation and conductance modulation with reduced energy consumption. One solution to operate metal oxide optoelectronic synapses with visible light inputs is to create their heterojunction structures,[42−44] which, however, involves highly sophisticated and elaborated fabrication procedures often causing nonuniform performances. Therefore, state-of-the-art optoelectronic synaptic devices are demanded, incorporating metal oxide semiconductors with small bandgap energies responding to broadband visible light spectra, which can intrinsically overcome all the aforementioned challenges.

Herein, we report on comprehensive optoelectronic synaptic characteristics of centimeter-scale tellurium dioxide (TeO_2) films facilely fabricated by a one-step chemical vapor deposition (CVD) method. The CVD-grown TeO_2 films are highly crystalline and yield a relatively small optical bandgap energy of 1.5 eV matching the visible spectrum range, verified by UV−visible absorbance characterization and its associated Tauc plot method. The as-grown TeO_2 films are delaminated and integrated onto flexible substrates, allowing for the inspection of their visible-light-driven optoelectronic synapses in mechanically deformable forms. Two-terminal flexible TeO_2 devices display strong broadband responsiveness and synaptic characteristics upon visible light illumination at a wide wavelength range of 405 to 940 nm. A comprehensive set of essential synaptic plasticity features are realized including paired-pulse facilitation (PPF), excitatory postsynaptic current (EPSC), long-term potentiation/depression (LTP/LTD), alteration from short-term to long-term memory (STM to LTM). Moreover, various application aspects of these flexible optoelectronic synaptic devices are investigated; i.e., synaptic simulation using artificial neural network (ANN) for letter/image recognition/processing, demonstration of logic functions for associative learning, as well as deep learning-driven prediction of input wavelength and Pavlovian conditioning experiment.

RESULTS AND DISCUSSION

TeO_2 Film Growth and Characterization. Centimeter-scale TeO_2 films are fabricated via a CVD process involving ambient oxidation and condensation of vaporized Te precursors. In short, Te powder filled in an alumina boat is placed upstream of a horizontal quartz tube furnace along with a clean silicon oxide/silicon (Si/SiO_2) wafer on the downstream side. Following evacuation and argon (Ar) gas purging, the quartz tube is heated up to 800 °C at a heating rate of 20 °C/min under a continuous flow of Ar gas at a rate of 150 standard cubic centimeters per minute (sccm), leading to the temperature of the Si/SiO_2 wafer close to 200 °C. After the CVD reaction of 30 min, the furnace is naturally cooled to room temperature. Growth condition details are presented in the Experimental Methods, and the schematic illustrations of the CVD growth process for TeO_2 films and their subsequent transfer via a thermal release tape (TRT) are displayed in Supporting Information, Figure S1. Figure 1a shows a photograph of as-grown TeO_2 film on SiO_2/Si with deposited

https://doi.org/10.1021/acsnano.4c04851
ACS Nano 2024, 18, 18635−18649

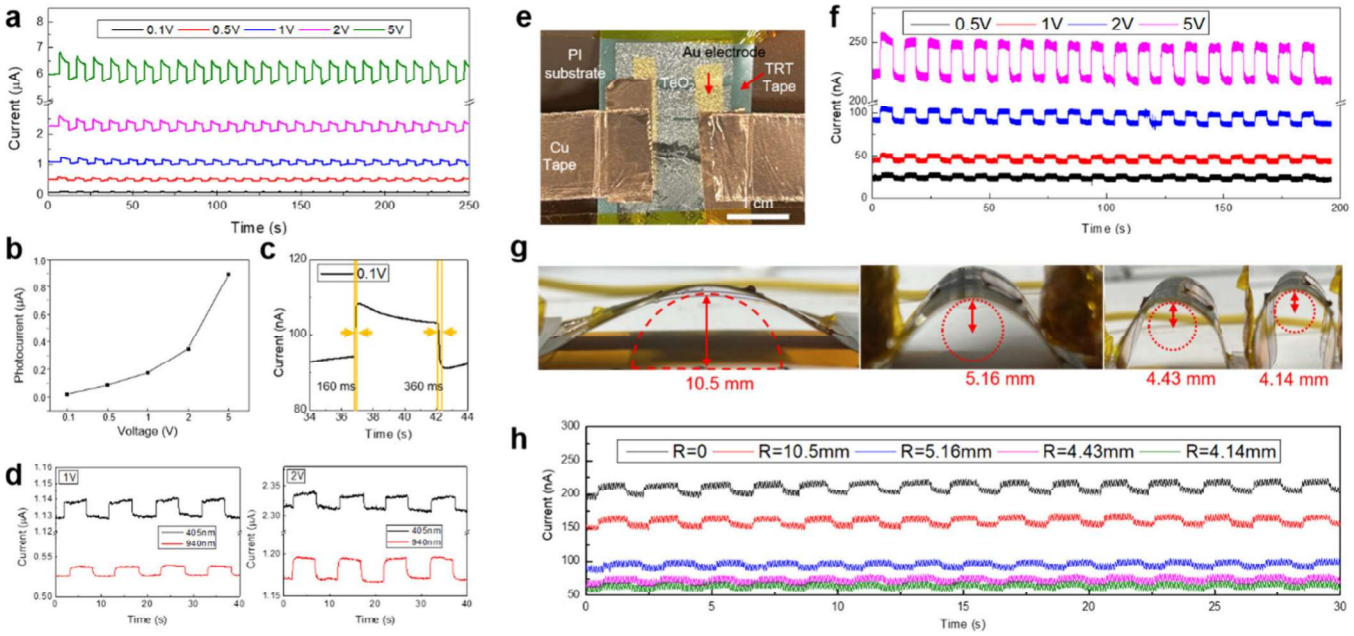

Figure 2. Broadband (405−940 nm wavelength) photoresponsiveness of TeO_2 on rigid/flexible substrates. (a) 625 nm wavelength photo responses of TeO_2 on rigid substrate. (b) Photocurrent vs applied voltage relationship. (c) Single response plot showing response/recovery times obtained from (a) under 0.1 V bias. (d) 405 and 940 nm wavelength photoresponsiveness of TeO_2 on rigid substrate. (e) Image of TeO_2 integrated on flexible substrate. (f) 625 nm wavelength photoresponsiveness of TeO_2 on flexible substrate. (g) Snapshot images of flexible device under mechanical bending with various bending radius values. (h) 625 nm wavelength photoresponsiveness of flexible TeO_2 corresponding to (g) under 5 V bias.

gold (Au) electrodes, revealing its large lateral dimension of > cm^2. Figure 1b presents the Raman spectroscopy characterization of the sample, displaying two noticeable peaks at 121 and 142 cm^{-1}, consistent with previous studies on TeO_2.[45−47] Figure 1c shows the X-ray photoelectron spectroscopy (XPS) spectra of Te binding energy obtained from the same sample, presenting 3d core-level characteristic peaks indicative of the oxidation state of Te, consistent with previous observations.[46] Corresponding XPS spectra of O_2 characteristic peaks are also presented in Supporting Information, Figure S2. Samples were further prepared at different CVD reaction temperatures; i.e., in a range of 750 and 950 °C, which yielded qualitatively similar XPS and Raman characteristics (Supporting Information, Figure S3). X-ray diffraction (XRD) patterns of the TeO_2 sample is presented in Figure 1d where the strong peak at 30° is indexed to tetragonal α-TeO_2 (102) [TeO_2 ICDD 42-1365 Indexing].[47−49] Also, all the remaining XRD peaks except for Te (102) peak (blue) well match with the previously reported characteristics of α-TeO_2 structure.[50,51] The corresponding XRD index card is displayed in Supporting Information, Figure S4a, which reveals great coherency with the experimental result in Figure 1d. Furthermore, the average crystallite size derived from the full width at half-maximum (fwhm) of XRD peaks is about 806 Å (Supporting Information, Figure S4b). The size determination is obtained from the major XRD peak of the TeO_2 (102) phase, which is positioned at 29.988°. Figure 1e shows the cross-sectional high-resolution transmission electron microscopy (HR-TEM) image of the prepared α-TeO_2 sample along with its atomic structure model (inset). The measured lattice fringe of 0.48 nm corresponds to the interplanar spacing of α-TeO_2 (100) planes.[49,52] Figure 1f depicts the selected area electron diffraction (SAED) patterns with indexed diffraction spots corresponding to α-TeO_2,[53] obtained from the sample in Figure 1e. Additional HRTEM images of other α-TeO_2 single-crystalline grains with (101) and (200) planes are presented in Supporting Information, Figure S5a, and a representative SAED pattern confirming the single crystallinity is displayed in Figure S5b. Furthermore, low-magnification TEM images of multiple large-sized polycrystalline grains and a representative SAED pattern confirming their polycrystallinity are presented in Supporting Information, Figure S5c,d. Figure 1g displays the energy dispersive X-ray spectrum (EDS) obtained from the same sample, revealing the stoichiometric ratio of Te:O ∼ 1:2, and its corresponding quantification analysis is presented in Supporting Information, Figure S5e. Following the structural and chemical characterizations, we inspected the electrical and optical properties of the CVD-grown TeO_2 films. To gain insights about their electronic structure and transport nature, we performed temperature variant current−voltage (I−V) measurements in a range of 300−475 K (Figure 1h). The TeO_2 films exhibit a noticeable increase in current with increasing temperature accompanied by Ohmic transport characteristics irrespective of the measured temperature, indicating their strong semiconducting nature.

Further inspection of the band structure of TeO_2 films was performed by UV−visible spectroscopy characterization. Figure 1i shows the UV−visible absorbance spectrum for the TeO_2 sample transferred onto an optically transparent glass substrate. The corresponding Tauc plot of $(\alpha h\nu)^2$ vs $h\nu$ derived from the absorbance spectrum is presented in Figure 1j. From the extrapolation of the linear plot (red dotted line), a direct band gap energy of 1.5 eV is verified by using $(\alpha h\nu)^n = A(h\nu - E_g)$, where h is Planck's constant, ν is the photon frequency, α is the absorption coefficient, E_g is the bandgap energy, and A is a proportionality constant.[54] This bandgap energy matches with the visible spectrum regime and is consistent with previous studies on α-TeO_2 prepared by other chemical methods,[54] concluding that our CVD-TeO_2 films do

https://doi.org/10.1021/acsnano.4c04851
ACS Nano 2024, 18, 18635−18649

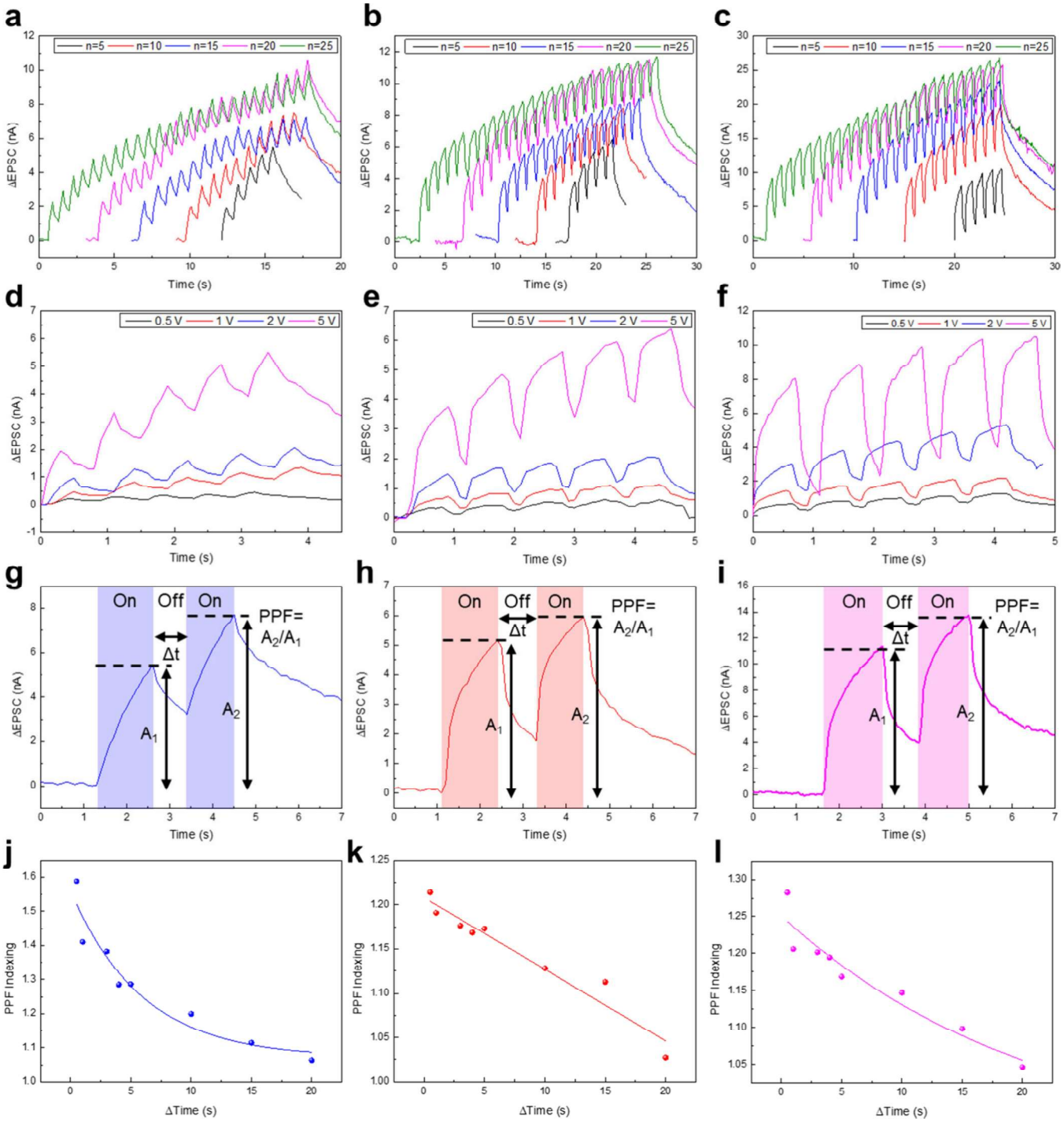

Figure 3. Optical synaptic plasticity characteristics of TeO_2. (a-c) STP and LTD of TeO_2 flexible device for pulse number of n = 5, 10, 15, 20, 25 under optical illumination at wavelengths of; (a) 405 nm, (b) 625 nm, and (c) 940 nm. (d-f) STP and LTD of TeO_2 flexible device for n = 5 under varying bias voltages at wavelengths of; (d) 405 nm, (e) 625 nm, and (f) 940 nm. (g-i) PPF indexwith time interval of Δt = 1 s obtained from wavelengths of; (g) 405 nm, (h) 625 nm, and (i) 940 nm. (j-l) PPF index vs Δt of 0.5, 1, 3, 4, 5, 10, 15, 20s obtained from wavelengths of; (j) 405 nm, (k) 625 nm, and (l) 940 nm.

not fall in the category of wide bandgap semiconductors. It is worth mentioning that the theoretically calculated bandgap energy values of α-TeO_2 are generally larger than those obtained with experiments including the present work.[55,56] One possible reason for this discrepancy is attributed to an introduction of unidentified defects into the material during its chemical synthesis, which might result in altering its electronic structures. Although such variations are not uncommon for any material synthesis, further investigations are needed to clarify the exact cause of the discrepancy. The value of n is varied by the electronic transition of materials (i.e., direct bandgap = 2, indirect bandgap = 1/2).[57]

Broadband Photoresponsiveness. Photoresponsiveness of the semiconducting TeO_2 films was investigated in their pristine state (i.e., as-grown on SiO_2/Si) as well as after their integration onto flexible substrates using TRT. The temporal

https://doi.org/10.1021/acsnano.4c04851
ACS Nano 2024, 18, 18635−18649

photoresponsiveness of TeO_2 on Si/SiO_2 and the corresponding broadband characteristics were characterized under optical illumination with various wavelengths of 405, 625, and 940 nm. Figure 2a shows the photocurrent generation of a sample under periodic optical illumination with 625 nm wavelength measured at various voltages of 0.1−5 V. It is observed that the current reversibly increases/decreases upon the application/termination of the illumination, respectively, which becomes more pronounced with increasing bias voltages. Figure 2b presents the bias voltage-dependent generation of photocurrent, I_{ph}, defined as $I_{ph} = I_{light} - I_{dark}$.[58−60] Figure 2c shows a representative plot of photocurrent generation and decay derived from Figure 2a for a single cycle of on/off illumination measured at 0.1 V, revealing small response/recovery times. Beyond the 625 nm wavelength-driven photoresponsiveness, the sample was also identified to be highly responsive to smaller (405 nm) as well as longer (940 nm) wavelengths up to the near-infrared (NIR) regime, as depicted in Figure 2d. Qualitatively similar photoresponsiveness was observed irrespective of the wavelength variation, confirming the broadband characteristics of the CVD-grown TeO_2 films. Representative data of NIR photoresponsiveness and its response/recovery times are shown in Supporting Information, Figure S6. As-grown TeO_2 films were delaminated off their Si/SiO_2 substrates by attaching TRT onto them and subsequent detachment. Figure 2e shows a photo of a TeO_2/TRT flexible device, which was additionally taped onto a polyimide (PI) substrate for electrical characterizations. Figure 2f shows the temporal photoresponsiveness of the TeO_2 flexible device under a periodic optical illumination at 625 nm wavelength measured under various bias voltages. Figure 2g depicts snapshot images of the same device under mechanical bending with systemically increasing bending radius values. Figure 2h shows the temporal photoresponsiveness of the flexible device measured at 5 V corresponding to Figure 2g, confirming its well-preserved photocurrent generation/decay characteristics despite the mechanical bending. It is noted that both base current and photocurrent steadily decrease with increasing bending radius values of 1−4 cm which correspond to the bending strain rate of 0.2262, 0.332, 0.4251, and 0.5192%, respectively.[61] The low variance in the strain values is attributed to the extremely small thickness (100 μm) of the underlying PI substrate,[62] and the relationship of strain vs photocurrent is depicted in Supporting Information, Figure S7.

Optical Synaptic Characteristics. Optical synaptic properties of TeO_2 films were characterized by potentiating them with consecutive instantaneous optical stimuli accompanied by their spontaneous conductivity decay. Artificial synapses behave similar to the memory learning/forgetting process of human brains as proposed by Atkinson and Shiffrin.[63] The organs responsible for various perceptions, such as visual, olfactory, gustatory, auditory, and tactile, receive their information and register it into sensory memories. The accepted information is converted to short-term memory (STM) lasting for a few seconds to minutes. When the maintained information frequently provokes the organs, the STM switches to long-term memory (LTM) stored for minutes to years. For the completion of the learning process, instantaneous stimuli must be repeatedly applied in few seconds, while longer time intervals lead to STM and memory loss/forgetting, suggesting that the stimulation frequency history critically governs the synaptic plasticity of neurons. This synaptic plasticity-driven STM-to-LTM transition is essential for artificial optical synapses, which can be demonstrated in TeO_2-based flexible devices through optical input modulations. Specifically, short optical pulses are continuously and frequently applied to the devices integrated with TRT to confirm their synaptic plasticity. The resulting synaptic characteristics are manifested by the devices' current response, called postsynaptic current (PSC), which is classified into excitatory (EPSC) and inhibitory (IPSC) determined by the current potentiation/depression, respectively.[64,65] Figures 3a-l present the comprehensive characteristics of optical synapses demonstrated with flexible TeO_2/TRT devices optically illuminated at three different wavelengths of 405, 625, and 940 nm, benefiting from their broadband responsiveness. Figure 3a shows the short-term plasticity (STP) of a device obtained under continuous illumination pulses at 405 nm wavelength with pulse number, n = 5, 10, 15, 20, 25 times and duration of 0.5s each. Similarly, Figures 3b and c show STP characteristics obtained with optical pulses at 625 and 940 nm, respectively. In all cases, long-term memory characteristics referred as long-term depression (LTD) are also observed once a significant amount of time passes after the application of optical pulses is completed. STP is a neural response property related to recognizing and processing input information, wherein the accepted information is easily forgotten.[66,67] STP and LTD characteristics of the flexible TeO_2/TRT device under various bias voltages (0.5, 1, 2, and 5 V) are displayed in Figures 3d-f. Specifically, the STP and LTD characteristics are defined at n = 5, introduced by optical illuminations at wavelengths of 405 nm (Figure 3d), 625 nm (Figure 3e), and 940 nm (Figure 3f), respectively. Paired-pulse facilitation (PPF) (or paired-pulse depression (PPD)) is another critical parameter to represent the essential STP characteristics of synaptic devices. Applying two consecutive and instantaneous stimuli to the devices results in an increase (or decrease) in their electrical conductance before they fully recover from the first stimulus. The ratio of EPSC (or IPSC) for the first (A_1) and second (A_2) stimulus is defined as PPF (or PPD) index.[68,69] Figures 3g−i shows the determination of the PPF index for the same device illuminated at wavelengths of 405 nm (Figure 3g), 625 nm (Figure 3h), and 940 nm (Figure 3i), respectively, turned on/off for 1s each. Another method to evaluate the plasticity of synaptic devices is plotting PPF/PPD index vs time interval (Δt) between two consecutive stimuli. Figures 3j−l shows typical PPF characteristics of the device under illuminations at 405 nm (Figure 3j), 625 nm (Figure 3k), and 940 nm (Figure 3l), respectively, obtained from eq 1[70]

$$\text{PPF index} = c_1 \cdot \exp\left(\frac{\Delta t}{\tau_1}\right) + c_2 \cdot \exp\left(\frac{\Delta t}{\tau_2}\right) + 1 \quad (1)$$

where Δt = 0.5, 1, 3, 4, 5, 10, 15, 20 s. It is worth mentioning that $TeO_2/SiO_2/Si$ rigid devices also exhibit qualitatively similar PPF characteristics, confirming that the observed optical synaptic characteristics originate from the TeO_2 films (Supporting Information, Figure S8). The relaxation time characteristics τ_1 (or, τ_2) represents the rapid (or, slow) phase of the PPF index, respectively, while the magnitude of the rapid (or, slow) phase is denoted by c_1 (or, c_2) which corresponds to the initial facilitation. In general, τ_2 is significantly larger than τ_1 in usual biological synapses, which is indicative of successive synaptic stimulation.[71] PPF characteristics are characterized by the nonvolatile modifica-

https://doi.org/10.1021/acsnano.4c04851
ACS Nano 2024, 18, 18635−18649

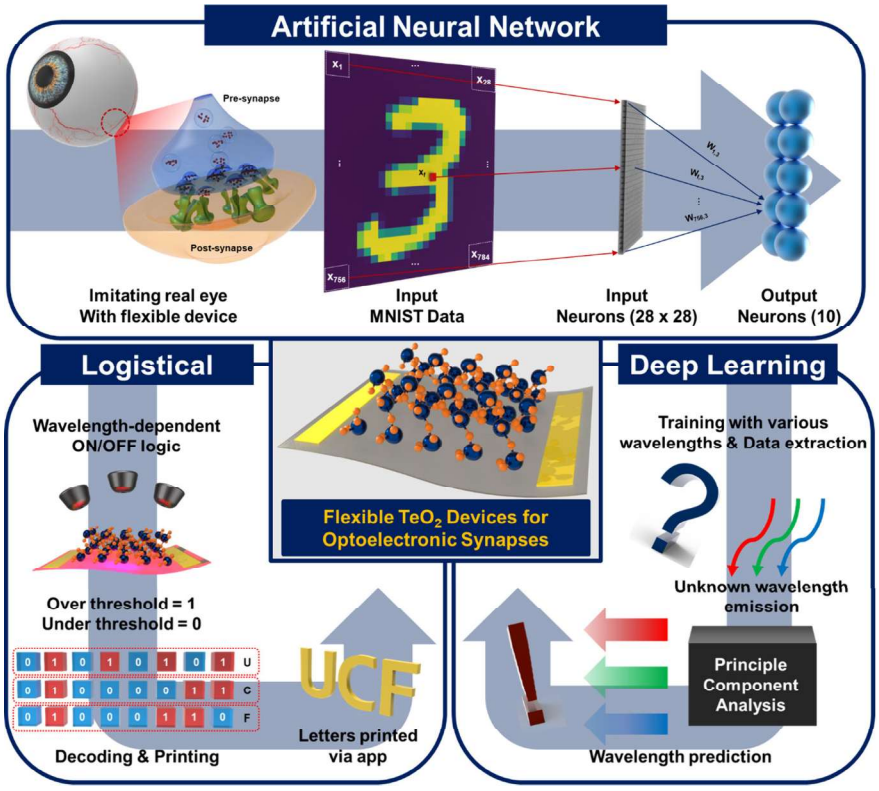

Figure 4. Overview of flexible TeO_2-enabled optoelectronic synapses in various applications.

tion of conductance in optical synapses, which enables to maintain PSC at a specific level even after the optical pulse illumination is terminated. Overall, Figure 3 confirms that TeO_2 devices demonstrate comprehensive features of STM, LTM, and the transition of STM-to-LTM at various wavelengths, essential for optical synapses in successfully mimicking the human brain memory process.

Here, we discuss the distinction in the photoresponsiveness characteristics between Figure 2 where no synaptic characteristics are observed and Figure 3 which exhibits notable synaptic features accompanying the memory effect, i.e. retention of photocurrents upon consecutive illuminations. This distinction is mainly attributed to the illumination conditions-driven persistent photoconductivity (PPC) effect of optically responsive semiconductors.[72,73] The broadband photoresponsiveness throughout Figure 2 is observed under illumination pulses with significantly longer duration times, i.e., >10 times than those adopted for the optical potentiation in Figure 3a–c. Upon observing the conventional photoresponsiveness in Figure 2, we systematically lowered the pulse illumination on/off durations in a way to maximize the emergence of the PPC effect in TeO_2 films. These shortened illumination intervals can efficiently sustain the residual photocurrent in the materials even after the termination of illumination hindering the full-recovery of their nonconductive states, which corresponds to the memory effect. The PPC effect is attributed to the defects-mediated alteration of the recombination dynamics of photoexcited carriers, commonly observed in semiconductors with sufficient surface defects capable of efficiently trapping the carriers.[74−77] Although it is challenging to exclusively pinpoint the exact cause of the PPC effect in our CVD-grown TeO_2 films, it is generally believed that the migration of surface oxygens inherent to metal oxide semiconductors plays a crucial role in causing the PPC effect in them, thereby optical synaptic characteristics.[78] The surface oxygens intrinsically present within metal oxides coupled with their imperfect crystallinity are attributed to introduce various midgap states within their bandgap, which causes the trapping and recombination of photoexcited electron−hole pairs accompanying their persistent decay.[78] Such characteristics become obviously more pronounced with metal oxides under short-duration optical pulses, which do not provide sufficient times for the full recovery of photoconduction. In other words, the slow recombination nature of the trapped charge carriers introduced by the surface defects enables the pulse-modulated optical potentiation accompanying synaptic plasticity features. Electrically driven depression characteristics are also understandable in the context of the charge trapping/detrapping mechanism influenced by externally applied electric fields. Negative voltage pulses can efficiently accelerate the elimination of the PPC effect, as demonstrated in Figures 5a-c. The proposed mechanism for this electrical depression is illustrated in Supporting Information, Figure S9. With increasing optical pulses, the conductivity of the optoelectronic device continues to increase due to the trapping-assisted slow annihilation of photoexcited carriers. Upon termination of the optical illumination, negative voltage pulses are applied to the device at its maximum electrical conductivity. Instantly, the trapped charge carriers by the optical potentiation start to become detrapped and released by the voltage pulses, leading to decreasing the conductivity. The detrapping of the charge carriers is further facilitated with increasing the number of voltage pluses, as extensively observed in previous studies.[24,29,44,65,76,79−81] Gradually, the trapped carriers are forcedly erased (i.e., accelerated recombination), and the conductivity

https://doi.org/10.1021/acsnano.4c04851
ACS Nano 2024, 18, 18635−18649

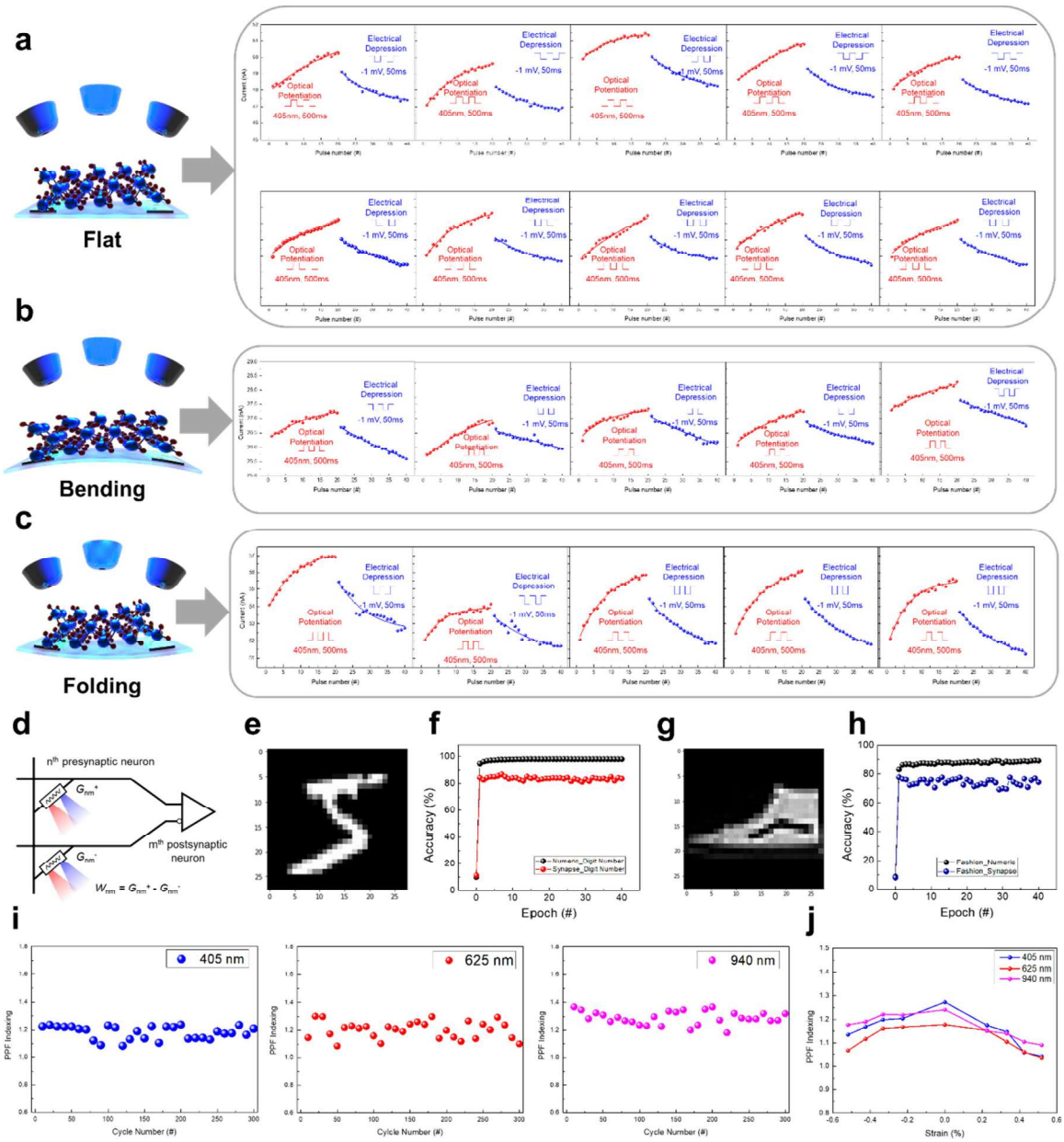

Figure 5. ANN applications demonstrating image recognition and mechanical robustness of a flexible TeO_2 optoelectronic device. (a-c) LTP/LTD characteristics of TeO_2 flexible device enabled by optical potentiation (wavelength: 405 nm, intensity: 15 W/m^2, interval: 0.5 s) and electrical depression (bias: −1 mV, interval: 50 ms) in three different states of; (a) flat, (b) bending, and (c) folding, respectively. (d) Diagram of the synaptic weight defined as the conductance difference of two adjacent optoelectronic synapses. (e) Trained Letter MNIST image example having 28 × 28 pixels. (f) Recognition accuracy of the image in (e) obtained from the device in (a). (g) Trained Fashion MNIST image example having 28 × 28 pixels. (h) Recognition accuracy of the image in (g) obtained from the device in (a). (i) PPF index of flexible TeO_2 device under cyclic bending/releasing tests corresponding to wavelengths of 405 nm (left), 625 nm (middle), and 940 nm (right). (j) Relationship between PPF index and strain ratio obtained at three different wavelengths.

of the device eventually returns to its initial state, completing the electrical depression.[82]

Overview of TeO_2 Optoelectronic Synapses in Various Applications. The broadband-responsive optical synaptic characteristics of TeO_2 films can be employed in a variety of optoelectronic synaptic applications. This study focuses on three different proof-of-concept demonstrations of ANN, logistical, and deep learning. Figure 4 shows the overall applications and their associated methodologies. (1) For the ANN applications, flexible TeO_2 devices are optically potentiated and electrically depressed through a large number of operations, from which a statistically reliable set of parameters essential for constructing ANN are extracted; these include synaptic weight nonlinearity, maximum/minimum conductance ratios, cycle-to-cycle variation, and device-to-device variation. In processing these data, neuromorphic simulations are conducted based on the Multi-Layer-Perceptron (MLP) neural network. Modified National Institute of Standards and Technology (MNIST) database images are trained and simulated, which demonstrates the pattern recognition ability of the devices. Details for the synaptic weight definition and the ANN algorithms will be explained in the next section. (2) For logistical applications, both rigid/flexible TeO_2 devices are illuminated at various

https://doi.org/10.1021/acsnano.4c04851
ACS Nano 2024, 18, 18635−18649

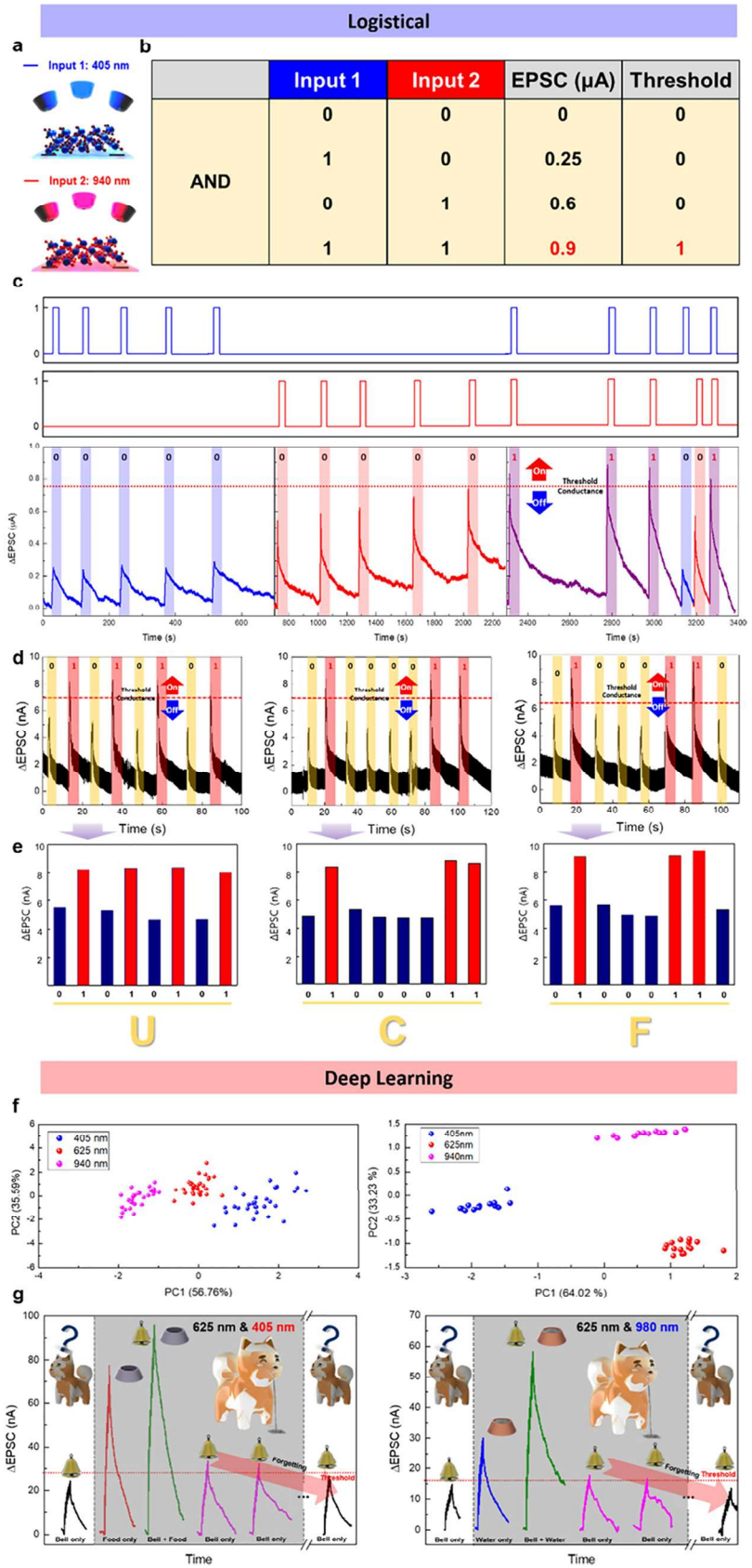

Figure 6. Logistical and deep learning-related applications of TeO_2 optoelectronic devices. (a-c) Boolean logic application implementations of TeO_2 on rigid substrates using inputs of 405 and 940 nm pulses; (a) schematics of operation principle, (b) table of AND logic operation conditions, and (c) experimental confirmation. (d, e) Demonstration of writing ASCII-converted letters of "UCF" based on the Boolean logic function with flexible TeO_2 devices; (d) two distinct conduction states of "on" and "off" realized with 405 and 940 nm illuminations, respectively, yielding letters of "U" (left), "C" (mid), and "F" (right). (e) Histograms of ΔEPSC employed to write "UCF" through

https://doi.org/10.1021/acsnano.4c04851
ACS Nano 2024, 18, 18635−18649

Figure 6. continued

encoding/decoding with ASCII binary codes, corresponding to "U" (left), "C" (mid), and "F" (right). (f, g) Demonstrations of deep learning-related applications using TeO_2 devices; (f) PCA plots for demonstration of conspicuous data discrimination such as identification of unknown wavelengths using TeO_2 films on rigid (left) and flexible (right) substrates. (g) Pavlov's conditioning demonstration using flexible TeO_2 devices illuminated with paired pulses of 625 nm/405 nm for bell/food (left) and 625 nm/980 nm for bell/water (right) stimuli, respectively.

wavelengths, which yields their wavelength-dependent threshold conductance. Based on the demonstration of the Boolean AND logic, each PSC corresponding to a specific wavelength is interpreted as "on" when it is higher than the threshold conductance and "off" when lower. This optically modulated "on" and "off" will be electrically encoded as "1" and "0" respectively, and the encoded series of 1/0 will be translated with ASCII binary codes. In this manner, writing of specifically desired ASCII letters will be possible, which will be demonstrated in the next section. (3) For the deep learning applications, prediction of an unknown wavelength illuminated onto the rigid/flexible devices will be demonstrated through their training with known wavelength characteristics. Specifically, the devices are illuminated at wavelengths of 405, 625, and 940 nm and resulting photoresponsiveness data are collected. The data of each wavelength should possess distinct characteristics which are utilized to interpret an unknown wavelength. The extracted data from various wavelengths are arranged using a principal component analysis (PCA) plotting method for the discrimination of characteristics. The features of each wavelength distributed and categorized through the PCA plot enable to discern the wavelength of unknown illumination. This concept of deep learning-based training will be further employed to demonstrate the well-known Pavlovian conditioning experiment.

Demonstration of ANN Applications with Flexible TeO_2 Devices via Corroborating Experimental Operation and Computational Simulation. By taking advantage of the features of optical synapses coupled with mechanical flexibility, we demonstrated the optoelectronic synaptic operations of TeO_2-based flexible devices and utilized them for ANN applications. Figure 5a-c shows LTP and LTD characteristics of the flexible device in three different physical states; i.e., flat (Figure 5a), bending (Figure 5b), and folding (Figure 5c), optically potentiated with optical pulses of 500 ms for each at 405 nm wavelength (illumination intensity: 15 W/m^2). In all cases, the device was electrically depressed with electrical pulses (−1 mV) for 50 ms, and the number of pulses is 20 for each of potentiation and depression. Tests were also conducted with 625 nm (illumination intensity: 140 W/m^2) and 940 nm (illumination intensity: 340 W/m^2) wavelengths in flat, bending, and folding states and the corresponding results are presented in Supporting Information, Figures S10 and S11, respectively. The nonlinearity factors for the obtained potentiation/depression curves are extracted from the following equations

$$G_{LTP} = B\cdot\left(1 - \exp\left(-\frac{P}{A_p}\right)\right) + G_{min} \quad (2)$$

$$G_{LTD} = -B\cdot\left(1 - \exp\left(\frac{P - P_{max}}{A_D}\right)\right) + G_{max} \quad (3)$$

$$B = (G_{max} - G_{min})/\left(1 - \exp\left(-\frac{P_{max}}{A_{P,D}}\right)\right) \quad (4)$$

Where G_{LTP}, G_{LTD} are the conductance values of LTP, LTD regions, G_{max}, G_{min} are the maximum, minimum conductance values in LTP, LTD, P is the number of pulses applied, A is the parameter representing the nonlinearity, and B is defined to simplify eqs 2, 3. The extracted potentiation nonlinearity factor values are in a range of 1.06 to 1.21, and depression nonlinearity factor values are in a range of −1.6 to −1.37, indicating that the device possesses desirable linearity. Figure 5d illustrates the synaptic weight definition as the conductance difference of two equal optical synapses ($W_{nm} = G_{nm}^{+} - G_{nm}^{-}$) which is updated by backpropagation.[8,38] For the demonstration of pattern/image recognition capability of the flexible device, a three-layered ANN (input, hidden, and output layers) was simulated to perform the learning of handwritten digits (28 × 28 pixels) adopted from the Modified National Institute of Standards and Technology (MNIST) (Figure 5e). For the simulation, 60,000 handwritten MNIST images were employed for training, and 10,000 images were used for testing evaluation. A fairly high accuracy of ∼85% was achieved in recognizing the images, as presented in Figure 5f. Additionally, we tested the device's capability in recognizing fashion MNIST images (Figure 5g), and its corresponding accuracy plot is presented in Figure 5h. Having confirmed the ANN applicability, we then inspected the mechanical robustness of the TeO_2 flexible device in retaining essential optoelectronic characteristics, even under severe mechanical deformation. The device was subjected to a repetitive application of bending/releasing for a total of 300 cycles with a bending radius of 10.5 mm, and its PPF index was obtained every 10 cycles. Figure 5i presents a trend of the PPF index for the same device tested under three different wavelengths of 405 nm (left), 625 nm (middle), and 940 nm (right). It is noteworthy that the device exhibits highly consistent PPF index values irrespective of the wavelength variation even for the prolonged cyclic endurance tests. We also characterized the PPF index characteristics with varying strain ratios, as presented in Figure 5j, wherein the positive and negative values correspond to the bending and folding states, respectively. PPF index values in a range of 1.1 to 1.3 are consistently observed throughout the strain change of ∼1.04%, which are well maintained for the three different tested wavelengths. The illumination interval for each wavelength was set to be 0.5 s for all tests.

Demonstration of Logistical and Deep Learning Applications with TeO_2 Devices. In addition to the ANN-based pattern recognition applications, additional applications of logistical and deep learning operations were also demonstrated with the same TeO_2 devices. The logical applications were implemented by demonstrating the threshold-conductance-enabled Boolean logic AND function and its associated ASCII-converted letter writing. TeO_2 devices in both flexible and rigid forms were employed to confirm that

https://doi.org/10.1021/acsnano.4c04851
ACS Nano 2024, 18, 18635−18649

the optical synaptic characteristics essential for the applications originate from the substrate-independent material properties of TeO_2 films. Under the illumination at two different wavelengths of 405 and 940 nm, the devices' reproducibility exhibits two distinct conductance responses with sufficient current contrasts. A threshold conductance is defined in between the distinct conductance response values, and the devices are set to be "on" state when the output current is higher than the threshold conductance and "off" when lower. Figure 6a illustrates the operation principle of Boolean AND logic where a TeO_2-based device exhibits photocurrent (EPSC) upon illumination with two independent optical pluses of 405 (input 1) and 940 nm (input 2). Figure 6b presents a table showing an all possible combination of pulse inputs and its corresponding average value of EPSC. It reveals that only the simultaneous application of both the inputs (i.e., "11") leads to the EPSC value becoming greater than a certain threshold current, which corresponds to turning the device on (i.e., "1"). Figure 6c displays a sequence of applied pulse inputs of 1 (top column) and 2 (mid column) and their corresponding photocurrent outcomes (bottom column). Beyond this Boolean AND function demonstration, we further substantiated the threshold-associated operation of our TeO_2 devices in flexible forms as well by demonstrating letter writing operations via ASCII binary codes. The on/off states obtained by the conductance data are translated through ASCII binary codes, assigning "on" state to "1" and "off" state to "0". These 1/0 sequences are grouped by eight components and subsequently interpreted to specifically desired letters according to the ASCII binary code.[21] The code was written in Python and feeding the experimentally obtained conductance data into it will write the desired letters through apps. The detailed letter writing process is introduced in Supporting Information, Video S1. Figures 6d shows representative sets of experimental conductance data employed to demonstrate writing letters of "UCF", wherein each figure corresponds to specific letters of "U" (left), "C" (mid), and "F" (right), respectively. Note that the threshold current of ∼7 nA is assigned for all cases, as the current responses from the two different wavelengths are clearly distinguishable across it. Figure 6e shows the histogram of ΔEPSC with eight sets of "1 (red)" and "0 (blue)" corresponding to Figure 6d, wherein their different letters of "U" (left), "C" (mid), and "F" (right) are ASCII-converted and printed, respectively. A demonstration of writing other letters such as "MSE" is also presented in Supporting Information, Figure S12. Lastly, the training ability of the device illuminated at various wavelengths is demonstrated by two different deep learning-related applications; (1) PCA plot construction and (2) Pavlovian conditioning. From the photoresponsiveness plots of TeO_2 devices on both rigid and flexible substrates as shown in Supporting Information, Figure S13, a large number of experimental data on three characteristic components; i.e., photocurrent, response time, and recovery time, are extracted for each illumination wavelength. These three components represent the specific characteristics of each wavelength, indicating that their determination will enable one to precisely identify the wavelength of the illumination sources. For this identification process, plotting the three different components (i.e., three-dimensional) in a single plot is essential, which is possible with the PCA method that linearly reduces the dimension of the data with improved visualization.[83] In this method, the data are linearly transformed into another coordinate system, where principal components are defined as the most significant variation in the data that are easily identifiable. The PCA is conducted on the set of three independently distributed variables, and the first principal component is a variable created as a linear combination of the original variables with respect to the highest variance. The second principal component represents the second highest variance, which can proceed by continuing three iterations until all variances are identified. Figure 6f depicts PCA plots of TeO_2 devices on rigid SiO_2/Si (left) and flexible PI (right) substrates, respectively. The PC1 and PC2 components represent the response and recovery time for rigid SiO_2/Si devices and the response time and photocurrent for flexible PI devices, respectively. The highly localized distribution of distinct PCA data for each figure denoted by different colors indicates the ability of the devices to predict and discern the kind of illumination sources even if they are exposed to illuminations of unknown characteristics. Figure 6g presents another example of the deep learning-based applications, i.e., Pavlovian conditioning (classical conditioning) experiment which represents an ability of associative learning that plays a vital role in cognitive functions.[84,85] In demonstrating the associative learning behavior of the flexible TeO_2 device, we simulate the Pavlov's dog experiment by optically training it with the situation that mimics the Pavlovian conditioning sequences using controlled illuminations; i.e., the device is initially exposed to 625 nm optical pulses repetitively, which function as the bell/conditioned stimulus to activate salivation/unconditioned responses. Subsequently, it is exposed to two different optical pulses of 405 nm (Figure 6g left) and 980 nm (Figure 6g right) wavelengths, which are defined as food/unconditioned and water/unconditioned stimuli, respectively. For each wavelength, 10 optical pulses are applied with an interval of 0.5 s. In the Pavlovian conditioning, ringing the bell only does not evoke any response from the dog while providing food or water stimulates the dog to respond by salivating. Then, simultaneously ringing the bell and providing food or water also stimulates the dog to respond and salivate. Once this training process is repeated and completed, the dog still responds to the bell ringing process even without food or water provided. After multiple sequences of the bell ringing stimulus process, the dog starts to forget the training and no longer responds to the bell-only process unless food or water are provided given a sufficient amount of time passed. In our measurements, the situation that the dog responds to the stimuli by salivating corresponds to that the device exhibits an output current exceeding a certain threshold conductance value set by the optical inputs. The device is initially trained with optical stimuli corresponding to the processes of bell-only (black curves in Figure 6g), food only (red curve in Figure 6g left), and water only (blue curve in Figure 6g right) upon illuminations at 625, 405, and 980 nm, respectively. Even after the training is completed, the device initially exhibits ΔEPSC values higher than the threshold conductance (red horizontal lines) under the bell-only process (i.e., 625 nm illumination), as manifested by the purple curves in both figures. Eventually, it exhibits ΔEPSC values lower than the threshold conductance upon the repetitive bell-only processes, which simulates the forgetting process of the Pavlovian's dog.

CONCLUSION

To summarize, we chemically grew semiconducting TeO_2 films with a moderately small bandgap energy and investigated their

https://doi.org/10.1021/acsnano.4c04851
ACS Nano 2024, 18, 18635−18649

artificial synapse applications. Pristine TeO_2 films exhibited broadband photoresponsiveness in a wavelength range of 405 to 940 nm owing to their visible spectrum-matching bandgap energy. Broadband-responsive optical synaptic characteristics such as wavelength-modulated synaptic plasticity was identified in TeO_2 films in both as-grown and mechanically flexible forms. Optically potentiated and electrically depressed TeO_2-based devices demonstrated optoelectronic synaptic characteristics capable of recognizing the intended patterns and images. Furthermore, a variety of proof-of-concept demonstrations were realized with these optoelectronic synaptic devices in the areas of logistical and deep learning applications. The study is believed to vastly broaden the versatility and opportunities of low-dimensional metal-oxides toward their integration into future neuromorphic systems.

EXPERIMENTAL METHODS

Growth of TeO_2 Films on Si/SiO_2 Substrates, Delamination of TeO_2 Films by TRT, and Metal Electrode Deposition. Te (tellurium powder, Sigma-Aldrich, 99.9%) was used as the precursor, and it was filled in an alumina boat positioned on the upstream of a horizontal quartz tube furnace (Lindberg/Blue M Mini-Mite). Si/SiO_2 substrate was cleaned with acetone and IPA and was subsequently positioned on the downstream of the tube furnace (temperature ~200 °C). The quartz tube was vacuumed to a base pressure of ~30 mTorr followed by purging with Ar gas for 10 min. The furnace was heated to 800 °C at a rate of 20 °C/min, and the Ar gas was continuously supplied at a flow rate of 150 standard cubic centimeters per minute (sccm) during the whole process. The reaction was kept for 30 min, and then the furnace was naturally cooled to room temperature. For the preparation of TeO_2 films-based flexible devices, TRT flexible substrates were directly integrated onto TeO_2 films as-grown on SiO_2/Si substrates by manual pressing. The TeO_2 film-attached TRT substrates were slowly peeled off the growth substrates. Both samples of TeO_2 films on Si/SiO_2 and TRT substrates were then deposited with Au electrodes via RF sputtering (deposition rate:15 nm/min, deposition time: 5 min)

Characterizations Using Raman, XPS, XRD, TEM, and UV–vis. Horiba LabRAM HR Evolution instrument was used for Raman characterization at room temperature with a 532 nm excitation laser. The XPS spectra were acquired using ESCALAB 250 (Thermo Fisher Scientific) in an ultrahigh vacuum condition (10^{-9} mBar). XRD (Empyrean; PANalytical) was conducted using a 2T-omega scan (10–80°2Th., step size 0.0130°2Th.) and Cu K-α (0.154060 nm) radiation. TEM/EDS images were obtained with a Talos F200X (Thermo Fisher Scientific) instrument which was operated at an acceleration voltage of 200 kV. An Evolution 220 UV–vis spectrometer was used for obtaining optical absorbance spectra in the wavelength range of 300–1100 nm.

Temperature-Dependent Conductance Measurement. The samples for temperature-dependent electrical conductance evaluations were fabricated by depositing Au electrodes onto as-grown TeO_2 films on Si/SiO_2 substrates (channel width = 0.5 cm and channel length = 2 cm). The temperature-dependent measurements were performed using Lake Shore Janis cryostat system and Agilent 4155A instrument. The temperature was controlled by MMR variable-temperature chamber with a K2000 temperature controller.

Photocurrent and Electrical Measurements. Optical illuminators of various wavelengths (405 nm; 100 mW cw laser diode light source, 625 nm; ThorlabsM625L4-C2, 940 nm; and ThorlabsM940L3-C1) were used for photocurrent measurements. A home-built probe station and a semiconductor parameter analyzer (Keysight B1500A) were used for electrical measurements.

Computation Simulations Using Optoelectronic Synaptic Device. Neuromorphic simulations were conducted based on the Multi-Layer-Perceptron (MLP) neural network. The handwritten digit images and Fashion images were composed of 28 × 28 pixels. 60,000 images each were trained and 10,000 images were tested for evaluation.

PCA Conduction Details for Wavelength Characteristic Discrimination.

1) Standardizing components: This step is to normalize the range of continuous starting variables to ensure each component contributes equally to the analysis. Initial standardization is crucial before conducting PCA because it is highly sensitive to the variances of the original variables. If the initial variables vary widely in their ranges, those with larger ranges will overshadow those with smaller ones (for instance, a variable ranging from 0 to 100 will overpower the one ranging from 0 to 1), leading to skewed results. Therefore, precisely scaling the data to similar levels is essential to avoid this issue. Each value of the variables is subtracted by their overall mean value and the difference of these value is divided by the standard deviation for the variables.

$$z = \frac{\text{value} - \text{mean}\ (m)}{\text{standard deviation}\ (\sigma)}$$

After the normalizing process, the variables are transformed to the same scales.

2) Covariance matrix computation: The purpose of this step is to examine how the variables in the input data set deviate from the mean in relation to each other, essentially to determine if any relationships exist between them. Often, variables are significantly correlated involving a redundancy of information. These correlations can be investigated by computing a covariance matrix. The covariance matrix is an $n \times n$ symmetric matrix (n is the number of dimensions) that contains the covariance for all possible pairs of initial variables. In our case, we used three variables (response time, recovery time, photocurrent), and the covariance matrix would be a 3 × 3 matrix arranged as the following:

$$\begin{bmatrix} Cov(a,a) & Cov(a,b) & Cov(a,c) \\ Cov(b,a) & Cov(b,b) & Cov(b,c) \\ Cov(c,a) & Cov(c,b) & Cov(c,c) \end{bmatrix}$$

The covariance of a variable with itself equals its variance (i.e., $\mathrm{Cov}(a, a) = Var(a)$) and the components on the main diagonal (row m × column m) of the covariance matrix represent the variances of each initial variable. Also, the covariance is commutative ($Cov(a, b) = Cov(b, a)$), and the components of the covariance matrix are symmetric about the main diagonal.

3) Calculation of the eigenvectors and eigenvalues of the covariance matrix to extract the principal components: Eigenvectors and eigenvalues are the linear algebra elements which are crucial to compute the covariance matrix in order to determine the principal components of the data. Eigenvectors and eigenvalues always come in pairs, meaning that eigenvectors possess eigenvalues and are identical to the number of dimensions of the data. In our case, we have 3 variables, 3 eigenvectors with 3 corresponding eigenvalues. Detailed processes of calculating eigenvalues, eigenvectors, and conducting PCA for TeO_2 devices are as follows. First, conduct a matrix (A) by estimating the response time, photocurrent, and recovery time of all 3 wavelengths. From 3 different wavelengths and 15 curves each, the matrix (A) would be 3 × 45 where rows are the variables and columns are the values of each variable. Then, conduct a matrix (B) where the components are the average value of each row, and subsequently subtract the matrix (A–B = C) from each other and transpose the matrix (C^T). After producing $C \times C^T$, multiply 44 (= 45–1) on the components (matrix D). Calculate the covariance matrix of D and then calculate the eigenvectors and eigenvalues for the covariant matrix. Since

https://doi.org/10.1021/acsnano.4c04851
ACS Nano 2024, 18, 18635–18649

there are three variables, three eigenvalues of PC1 (response time), PC2 (photocurrent), and PC3 (recovery time) exist (in case of the flexible substrate). The larger two eigenvalues are the modified x- and y-axis. Produce a modified 3 × 3 matrix (E) whose components are the eigenvectors of the two large eigenvalues and the residue components as 0. Next, conduct a modified matrix (F) by multiplying 44 on matrix C and transposing. Finally, multiply matrix F (45 × 3) and E (3 × 3), which are the plots of the modified x and y-axis.

ASSOCIATED CONTENT

Supporting Information

The Supporting Information is available free of charge at https://pubs.acs.org/doi/10.1021/acsnano.4c04851.

Schematic illustrations of CVD process and TRT-assisted layer transfer (S1), XPS O 1s of sample (S2), XPS and Raman of samples grown at various temperatures (S3), theoretical XRD card and crystallite size determination (S4), additional HRTEM/SAED patterns and EDS spectrum (S5), NIR response of device (S6), strain-photocurrent relationship plot (S7), optical synaptic plasticity of rigid sample (S8), illustration of device operation based on charge trap/detrap mechanism (S9), LTP/LTD characteristics of flexible device in flat, bending, folding states under 625 nm illumination (S10), LTP/LTD characteristics of flexible device in flat, bending, folding states under 940 nm illumination (S11), logistical applications for writing other letters (S12), photoresponsiveness of rigid and flexible devices for wavelengths of 405, 625, 940 nm (S13) (PDF)

Movie of encoding and decoding electrical conductance information to letters via application (MP4)

AUTHOR INFORMATION

Corresponding Author

Yeonwoong Jung − *NanoScience Technology Center, University of Central Florida, Orlando, Florida 32826, United States; Department of Materials Science and Engineering and Department of Electrical and Computer Engineering, University of Central Florida, Orlando, Florida 32816, United States;* orcid.org/0000-0001-6042-5551; Email: yeonwoong.jung@ucf.edu

Authors

Chung Won Lee − *NanoScience Technology Center, University of Central Florida, Orlando, Florida 32826, United States*

Changhyeon Yoo − *NanoScience Technology Center, University of Central Florida, Orlando, Florida 32826, United States*

Sang Sub Han − *NanoScience Technology Center, University of Central Florida, Orlando, Florida 32826, United States*

Yu-Jin Song − *Department of Materials Science and Engineering, Dong-A University, Busan 49315, Republic of Korea*

Seung Ju Kim − *The Department of Electrical and Computer Engineering, University of Southern California, Los Angeles, California 90089, United States*

Jung Han Kim − *Department of Materials Science and Engineering, Dong-A University, Busan 49315, Republic of Korea;* orcid.org/0000-0002-6678-2282

Complete contact information is available at: https://pubs.acs.org/10.1021/acsnano.4c04851

Author Contributions

C.W.L. conceived the project idea under the guidance of Y.J. C.W.L. prepared the samples and conducted the photocurrent and optical synapses tests and computational simulations. C.Y. assisted the temperature-dependent conductivity measurements and the fabrication of flexible devices. S.S.H. helped with the XPS characterization. Y.J.S. performed the XRD, TEM characterizations under the guidance of J.H.K. S.J.K. conducted the neuromorphic simulation. C.W.L and Y.J. wrote the manuscript with inputs from all authors.

Notes

The authors declare no competing financial interest.

ACKNOWLEDGMENTS

Y.J. acknowledges financial support from the US National Science Foundation (CAREER: 2142310). S.S.H. acknowledges financial support from the Preeminent Postdoctoral Program (P3) at UCF. J.H.K. acknowledges support from the Ministry of Science and ICT (Project Number: 2024-22030006-00), and Commercialization Promotion Agency for R&D Outcomes (COMPA).

REFERENCES

(1) Wu, C.; Kim, T. W.; Choi, H. Y.; Strukov, D. B.; Yang, J. J. Flexible Three-Dimensional Artificial Synapse Networks with Correlated Learning and Trainable Memory Capability. *Nat. Commun.* **2017**, *8*, 752.

(2) Liu, C.; Yan, X.; Song, X.; Ding, S.; Zhang, D. W.; Zhou, P. A Semi-Floating Gate Memory Based on van der Waals Heterostructures for Quasi-Non-Volatile Applications. *Nat. nanotechnol.* **2018**, *13*, 404−410.

(3) Manipatruni, S.; Nikonov, D. E.; Young, I. A. Beyond CMOS Computing with Spin and Polarization. *Nat. Phys.* **2018**, *14*, 338−343.

(4) Kumar, M.; Kim, J.; Wong, C.-P. Transparent and Flexible Photonic Artificial Synapse with Piezo-Phototronic Modulator: Versatile Memory Capability and Higher Order Learning Algorithm. *Nano Energy* **2019**, *63*, 103843.

(5) Yoo, C.; Ko, T.-J.; Kaium, M. G.; Martinez, R.; Islam, M. M.; Li, H.; Kim, J. H.; Cao, J.; Acharya, M.; Roy, T.; Jung, Y. A Minireview on 2D Materials-Enabled Optoelectronic Artificial Synaptic Devices. *APL Mater.* **2022**, *10*, 070702.

(6) Wang, T. Y.; Meng, J. L.; He, Z. Y.; Chen, L.; Zhu, H.; Sun, Q. Q.; Ding, S. J.; Zhou, P.; Zhang, D. W. Ultralow Power Wearable Heterosynapse with Photoelectric Synergistic Modulation. *Adv. Sci.* **2020**, *7*, 1903480.

(7) Duan, N.; Li, Y.; Chiang, H.-C.; Chen, J.; Pan, W.-Q.; Zhou, Y.-X.; Chien, Y.-C.; He, Y.-H.; Xue, K.-H.; Liu, G.; et al. An Electro-Photo-Sensitive Synaptic Transistor for Edge Neuromorphic Visual Systems. *Nanoscale* **2019**, *11*, 17590−17599.

(8) Seo, S.; Kang, B.-S.; Lee, J.-J.; Ryu, H.-J.; Kim, S.; Kim, H.; Oh, S.; Shim, J.; Heo, K.; Oh, S.; Park, J.-H. Artificial van der Waals Hybrid Synapse and Its Application to Acoustic Pattern Recognition. *Nat. commun.* **2020**, *11*, 3936.

(9) Yu, S.; Gao, B.; Fang, Z.; Yu, H.; Kang, J.; Wong, H. S. P. A Low Energy Oxide-Based Electronic Synaptic Device for Neuromorphic Visual Systems with Tolerance to Device Variation. *Adv. Mater.* **2013**, *25*, 1774−1779.

(10) Seo, S.; Jo, S.-H.; Kim, S.; Shim, J.; Oh, S.; Kim, J.-H.; Heo, K.; Choi, J.-W.; Choi, C.; Oh, S.; et al. Artificial Optic-Neural Synapse for Colored and Color-Mixed Pattern Recognition. *Nat. Commun.* **2018**, *9*, 5106.

(11) Zhou, F.; Zhou, Z.; Chen, J.; Choy, T. H.; Wang, J.; Zhang, N.; Lin, Z.; Yu, S.; Kang, J.; Wong, H.-S. P.; Chai, Y. Optoelectronic Resistive Random Access Memory for Neuromorphic Vision Sensors. *Nat. nanotechnol.* **2019**, *14*, 776−782.

(12) Dai, S.; Zhao, Y.; Wang, Y.; Zhang, J.; Fang, L.; Jin, S.; Shao, Y.; Huang, J. Recent Advances in Transistor-Based Artificial Synapses. *Adv. Funct. Mater.* **2019**, *29*, 1903700.
(13) Li, J.; Ge, C.; Du, J.; Wang, C.; Yang, G.; Jin, K. Reproducible Ultrathin Ferroelectric Domain Switching for High-Performance Neuromorphic Computing. *Adv. Mater.* **2020**, *32*, 1905764.
(14) Guo, T.; Pan, K.; Jiao, Y.; Sun, B.; Du, C.; Mills, J. P.; Chen, Z.; Zhao, X.; Wei, L.; Zhou, Y. N.; Wu, Y. A. Versatile Memristor for Memory and Neuromorphic Computing. *Nanoscale Horiz.* **2022**, *7*, 299−310.
(15) Wang, B.; Wang, X.; Wang, E.; Li, C.; Peng, R.; Wu, Y.; Xin, Z.; Sun, Y.; Guo, J.; Fan, S.; et al. Monolayer MoS_2 Synaptic Transistors for High-Temperature Neuromorphic Applications. *Nano Lett.* **2021**, *21*, 10400−10408.
(16) Singh, P.; Baek, S.; Yoo, H. H.; Niu, J.; Park, J.-H.; Lee, S. Two-Dimensional CIPS-InSe van der Waal Heterostructure Ferroelectric Field Effect Transistor for Nonvolatile Memory Applications. *ACS Nano* **2022**, *16*, 5418−5426.
(17) Yang, C. M.; Chen, T. C.; Verma, D.; Li, L. J.; Liu, B.; Chang, W. H.; Lai, C. S. Bidirectional All-Optical Synapses Based on a 2D Bi_2O_2Se/Graphene Hybrid Structure for Multifunctional Optoelectronics. *Adv. Funct. Mater.* **2020**, *30*, 2001598.
(18) Ahmed, T.; Kuriakose, S.; Mayes, E. L.; Ramanathan, R.; Bansal, V.; Bhaskaran, M.; Sriram, S.; Walia, S. Optically Stimulated Artificial Synapse Based on Layered Black Phosphorus. *Small* **2019**, *15*, 1900966.
(19) Li, H.; Jiang, X.; Ye, W.; Zhang, H.; Zhou, L.; Zhang, F.; She, D.; Zhou, Y.; Han, S.-T. Fully Photon Modulated Heterostructure for Neuromorphic Computing. *Nano Energy* **2019**, *65*, 104000.
(20) Meng, J.; Wang, T.; Zhu, H.; Ji, L.; Bao, W.; Zhou, P.; Chen, L.; Sun, Q.-Q.; Zhang, D. W. Integrated In-Sensor Computing Optoelectronic Device for Environment-Adaptable Artificial Retina Perception Application. *Nano Lett.* **2022**, *22*, 81−89.
(21) Li, Y.; Wang, J.; Yang, Q.; Shen, G. Flexible Artificial Optoelectronic Synapse Based on Lead-Free Metal Halide Nanocrystals for Neuromorphic Computing and Color Recognition. *Adv. Sci.* **2022**, *9*, 2202123.
(22) Ji, R.; Feng, G.; Jiang, C.; Tian, B.; Luo, C.; Lin, H.; Tang, X.; Peng, H.; Duan, C. G. Fully Light-Modulated Organic Artificial Synapse with the Assistance of Ferroelectric Polarization. *Adv. Electron. Mater.* **2022**, *8*, 2101402.
(23) Hao, D.; Yang, Z.; Huang, J.; Shan, F. Recent Developments of Optoelectronic Synaptic Devices Based on Metal Halide Perovskites. *Adv. Funct. Mater.* **2023**, *33*, 2211467.
(24) Liu, K.; Zhang, T.; Dang, B.; Bao, L.; Xu, L.; Cheng, C.; Yang, Z.; Huang, R.; Yang, Y. An Optoelectronic Synapse Based on α-In_2Se_3 with Controllable Temporal Dynamics for Multimode and Multiscale Reservoir Computing. *Nat. Electron.* **2022**, *5*, 761−773.
(25) Zha, J.; Shi, S.; Chaturvedi, A.; Huang, H.; Yang, P.; Yao, Y.; Li, S.; Xia, Y.; Zhang, Z.; Wang, W.; et al. Electronic/Optoelectronic Memory Device Enabled by Tellurium-Based 2D van der Waals Heterostructure for In-Sensor Reservoir Computing at the Optical Communication Band. *Adv. Mater.* **2023**, *35*, 2211598.
(26) Li, Q.; Wang, T.; Fang, Y.; Hu, X.; Tang, C.; Wu, X.; Zhu, H.; Ji, L.; Sun, Q.-Q.; Zhang, D. W.; Chen, L. Ultralow Power Wearable Organic Ferroelectric Device for Optoelectronic Neuromorphic Computing. *Nano Lett.* **2022**, *22*, 6435−6443.
(27) Yin, L.; Huang, W.; Xiao, R.; Peng, W.; Zhu, Y.; Zhang, Y.; Pi, X.; Yang, D. Optically Stimulated Synaptic Devices Based on the Hybrid Structure of Silicon Nanomembrane and Perovskite. *Nano Lett.* **2020**, *20*, 3378−3387.
(28) Sun, Y.; Ding, Y.; Xie, D.; Xu, J.; Sun, M.; Yang, P.; Zhang, Y. Optogenetics-Inspired Neuromorphic Optoelectronic Synaptic Transistors with Optically Modulated Plasticity. *Adv. Opt. Mater.* **2021**, *9*, 2002232.
(29) Ma, F.; Zhu, Y.; Xu, Z.; Liu, Y.; Zheng, X.; Ju, S.; Li, Q.; Ni, Z.; Hu, H.; Chai, Y.; et al. Optoelectronic Perovskite Synapses for Neuromorphic Computing. *Adv. Funct. Mater.* **2020**, *30*, 1908901.
(30) Wang, W.; Gao, S.; Li, Y.; Yue, W.; Kan, H.; Zhang, C.; Lou, Z.; Wang, L.; Shen, G. Artificial Optoelectronic Synapses Based on TiN_xO_2−x/MoS_2 Heterojunction for Neuromorphic Computing and Visual System. *Adv. Funct. Mater.* **2021**, *31*, 2101201.
(31) Yin, X.; Wang, Y.; Chang, T.-h.; Zhang, P.; Li, J.; Xue, P.; Long, Y.; Shohet, J. L.; Voyles, P. M.; Ma, Z.; Wang, X. Memristive Behavior Enabled by Amorphous−Crystalline 2D Oxide Heterostructure. *Adv. Mater.* **2020**, *32*, 2000801.
(32) Huang, C.-H.; Chang, H.; Yang, T.-Y.; Wang, Y.-C.; Chueh, Y.-L.; Nomura, K. Artificial Synapse Based on a 2D-SnO_2 Memtransistor with Dynamically Tunable Analog Switching for Neuromorphic Computing. *ACS Appl. Mater. Interfaces.* **2021**, *13*, 52822−52832.
(33) Krishnamurthi, V.; Ahmed, T.; Mohiuddin, M.; Zavabeti, A.; Pillai, N.; McConville, C. F.; Mahmood, N.; Walia, S. A Visible-Blind Photodetector and Artificial Optoelectronic Synapse Using Liquid-Metal Exfoliated ZnO Nanosheets. *Adv. Opt. Mater.* **2021**, *9*, 2100449.
(34) Zhou, K.; Shang, G.; Hsu, H. H.; Han, S. T.; Roy, V. A.; Zhou, Y. Emerging 2D Metal Oxides: from Synthesis to Device Integration. *Adv. Mater.* **2023**, *35*, 2207774.
(35) Nomura, K.; Ohta, H.; Takagi, A.; Kamiya, T.; Hirano, M.; Hosono, H. Room-Temperature Fabrication of Transparent Flexible Thin-Film Transistors Using Amorphous Oxide Semiconductors. *Nature* **2004**, *432*, 488−492.
(36) Nomura, K.; Ohta, H.; Ueda, K.; Kamiya, T.; Hirano, M.; Hosono, H. Thin-Film Transistor Fabricated in Single-Crystalline Transparent Oxide Semiconductor. *Science* **2003**, *300*, 1269−1272.
(37) Kim, Y.-H.; Heo, J.-S.; Kim, T.-H.; Park, S.; Yoon, M.-H.; Kim, J.; Oh, M. S.; Yi, G.-R.; Noh, Y.-Y.; Park, S. K. Flexible Metal-Oxide Devices Made by Room-Temperature Photochemical Activation of Sol−Gel Films. *Nature* **2012**, *489*, 128−132.
(38) Kim, J.; Song, S.; Lee, J. M.; Nam, S.; Kim, J.; Hwang, D. K.; Park, S. K.; Kim, Y. H. Metal-Oxide Heterojunction Optoelectronic Synapse and Multilevel Memory Devices Enabled by Broad Spectral Photocarrier Modulation. *Small* **2023**, *19*, 2301186.
(39) Kim, J.; Song, S.; Kim, H.; Yoo, G.; Cho, S. S.; Kim, J.; Park, S. K.; Kim, Y.-H. Light-Stimulated Artificial Photonic Synapses Based on Solution-Processed In-Sn-Zn-O Transistors for Neuromorphic Applications. *J. Alloys Compd.* **2022**, *903*, 163873.
(40) Wu, Q.; Wang, J.; Cao, J.; Lu, C.; Yang, G.; Shi, X.; Chuai, X.; Gong, Y.; Su, Y.; Zhao, Y.; et al. Photoelectric Plasticity in Oxide Thin Film Transistors with Tunable Synaptic Functions. *Adv. Electron. Mater.* **2018**, *4*, 1800556.
(41) Hong, S.; Cho, H.; Kang, B. H.; Park, K.; Akinwande, D.; Kim, H. J.; Kim, S. Neuromorphic Active Pixel Image Sensor Array for Visual Memory. *ACS Nano* **2021**, *15*, 15362−15370.
(42) Lv, Z.; Wang, Y.; Chen, J.; Wang, J.; Zhou, Y.; Han, S.-T. Semiconductor Quantum Dots for Memories and Neuromorphic Computing Systems. *Chem. Rev.* **2020**, *120*, 3941−4006.
(43) Kim, S. H.; Baek, G. W.; Yoon, J.; Seo, S.; Park, J.; Hahm, D.; Chang, J. H.; Seong, D.; Seo, H.; Oh, S.; et al. A Bioinspired Stretchable Sensory-Neuromorphic System. *Adv. Mater.* **2021**, *33*, 2104690.
(44) Wang, Y.; Lv, Z.; Chen, J.; Wang, Z.; Zhou, Y.; Zhou, L.; Chen, X.; Han, S. T. Photonic Synapses Based on Inorganic Perovskite Quantum Dots for Neuromorphic Computing. *Adv. Mater.* **2018**, *30*, 1802883.
(45) Mirgorodsky, A.; Merle-Méjean, T.; Champarnaud, J.-C.; Thomas, P.; Frit, B. Dynamics and Structure of TeO_2 Polymorphs: Model Treatment of Paratellurite and Tellurite; Raman Scattering Evidence for New γ-and δ-Phases. *J. Phys. Chem. Solids* **2000**, *61*, 501−509.
(46) Hesabizadeh, T.; Hicks, E.; Medina Cruz, D.; Bourdo, S. E.; Watanabe, F.; Bonney, M.; Nichols, J.; Webster, T. J.; Guisbiers, G. Synthesis of "Naked" TeO_2 Nanoparticles for Biomedical Applications. *ACS omega* **2022**, *7*, 23685−23694.
(47) Shen, Y.; Wang, K.; Liu, H.; Chen, L.; Jin, Z.; Yan, S. Rapid and Efficient NO_2 Sensing Performance of TeO_2 Nanowires. *Sensors* **2023**, *23*, 9097.

https://doi.org/10.1021/acsnano.4c04851
ACS Nano 2024, 18, 18635−18649

(48) Filippo, E.; Micocci, G.; Tepore, A.; Siciliano, T. Fabrication of α-TeO_2 Smooth and Beaded Microwires by Thermal Evaporation Method. *J. Cryst. Growth* **2011**, *336*, 101−105.
(49) Jin, C.-H.; Park, S.-H.; Kim, H.-S.; Lee, C.-M. Enhanced Gas Sensing Properties of Pt-Loaded TeO_2 Nanorods. *Bull. Korean Chem. Soc.* **2012**, *33*, 1851−1855.
(50) Santos, G.; Braghirolli, A.; Batista, J. A Feasibility Study for Routine Production of 124I by (α, xn) Reactions on NatSb and 121Sb at the IEN's CV-28 cyclotron: current status. https://www.researchgate.net/publication/306018789_A_feasibility_study_for_routine_production_of_124_I_by_alphaxn_reactions_on_nat_Sb_and_121_Sb_at_the_IEN's_CV-28_cyclotron_current_status (accessed 2024-06-17).
(51) Aydin, N.; Arslan, M. E.; Sonmez, E. S.; Turkez, H. Cytotoxicity Analysis of Tellurium Dioxide Nanoparticles on Cultured Human Pulmonary Alveolar Epithelial and Peripheral Blood Cell Cultures. *Biomed. Res. India* **2017**, *28*, 3300−3304.
(52) Albukhari, S. M.; Shawky, A. Ag/Ag_2O-Decorated Sol-Gel-Processed TeO_2 Nanojunctions for Enhanced H_2 Production Under Visible Light. *J. Mol. Liq.* **2021**, *336*, 116870.
(53) Shen, Y.; Fan, A.; Wei, D.; Gao, S.; Liu, W.; Han, C.; Cui, B. A Low-Temperature n-propanol Gas Sensor Based on TeO_2 Nanowires as the Sensing Layer. *RSC Adv.* **2015**, *5*, 29126−29130.
(54) Kariper, İ. A. Optical Properties and Surface Energy of Tellurium Oxide Thin Film. *J. Opt.* **2018**, *47*, 504−510.
(55) Li, Y.; Fan, W.; Sun, H.; Cheng, X.; Li, P.; Zhao, X. Structural, Electronic, and Optical Properties of α, β, and γ-TeO_2. *J. Appl. Phys.* **2010**, *107*, 093506.
(56) Roginskii, E.; Kuznetsov, V.; Smirnov, M.; Noguera, O.; Duclère, J.-R.; Colas, M.; Masson, O.; Thomas, P. Comparative Analysis of the Electronic Structure and Nonlinear Optical Susceptibility of α-TeO_2 and β-TeO_3 Crystals. *J. Phys. Chem. C* **2017**, *121*, 12365−12374.
(57) Viezbicke, B. D.; Patel, S.; Davis, B. E.; Birnie, D. P., III Evaluation of the Tauc Method for Optical Absorption Edge Determination: ZnO Thin Films as a Model System. *Phys. Status Solidi B Basic Res.* **2015**, *252*, 1700−1710.
(58) Shawkat, M. S.; Hafiz, S. B.; Islam, M. M.; Mofid, S. A.; Al Mahfuz, M. M.; Biswas, A.; Chung, H.-S.; Okogbue, E.; Ko, T.-J.; Chanda, D.; et al. Scalable van der Waals Two-Dimensional $PtTe_2$ Layers Integrated Onto Silicon for Efficient Near-to-Mid Infrared Photodetection. *ACS Appl. Mater. Interfaces.* **2021**, *13*, 15542−15550.
(59) Han, S. S.; Shawkat, M. S.; Lee, Y. H.; Park, G.; Li, H.; Chung, H.-S.; Yoo, C.; Mofid, S. A.; Sattar, S.; Choudhary, N.; et al. Wafer-Scale Anion Exchange Conversion of Nonlayered PtS Films to van der Waals Two-Dimensional $PtTe_2$ Layers with Negative Photoresponsiveness. *Chem. Mater.* **2022**, *34*, 6996−7005.
(60) Shawkat, M. S.; Han, S. S.; Chung, H. S.; Mofid, S. A.; Yoo, C.; Jung, Y. Wafer-Scale van der Waals Assembly of Free-Standing Near Atom Thickness Hetero-Membranes for Flexible Photo-Detectors. *Adv. Electron. Mater.* **2021**, *7*, 2100395.
(61) Ding, R.; Lyu, Y.; Wu, Z.; Guo, F.; Io, W. F.; Pang, S. Y.; Zhao, Y.; Mao, J.; Wong, M. C.; Hao, J. Effective Piezo-Phototronic Enhancement of Flexible Photodetectors Based on 2D Hybrid Perovskite Ferroelectric Single-Crystalline Thin-Films. *Adv. Mater.* **2021**, *33*, 2101263.
(62) Yoo, C.; Han, S. S.; Okogbue, E.; Bae, T.-S.; Jang, J. H.; Cao, J.; Chung, H.-S.; Jung, Y. Humidity-Driven High-Performance Electrothermal Actuation of Vertically Stacked 2D $PtTe_2$ Layers/Cellulose Nanofibers. *Adv. Intell. Syst.* **2023**, *5*, 2200269.
(63) Atkinson, R. C.; Shiffrin, R. M. Human Memory: A Proposed System and Its Control Processes. In *Psychology of Learning and Motivation*, Vol. *2*; Spence, K. W., Spence, J. T., Eds.; Elsevier, 1968; pp 89−195.
(64) Guo, Y.; Wu, F.; Dun, G.-H.; Cui, T.; Liu, Y.; Tan, X.; Qiao, Y.; Lanza, M.; Tian, H.; Yang, Y.; Ren, T.-L. Electrospun Nanofiber-Based Synaptic Transistor with Tunable Plasticity for Neuromorphic Computing. *Adv. Funct. Mater.* **2023**, *33*, 2208055.
(65) Liu, Y.; Wu, Y.; Han, H.; Wang, Y.; Peng, R.; Liu, K.; Yi, D.; Nan, C. W.; Ma, J. $CuInP_2S_6$-Based Electronic/Optoelectronic Synapse for Artificial Visual System Application. *Adv. Funct. Mater.* **2024**, *34*, 2306945.
(66) Chen, X.; Chen, B.; Jiang, B.; Gao, T.; Shang, G.; Han, S. T.; Kuo, C. C.; Roy, V. A.; Zhou, Y. Nanowires for UV−vis−IR Optoelectronic Synaptic Devices. *Adv. Funct. Mater.* **2023**, *33*, 2208807.
(67) Wang, Y.; Yin, L.; Huang, W.; Li, Y.; Huang, S.; Zhu, Y.; Yang, D.; Pi, X. Optoelectronic Synaptic Devices for Neuromorphic Computing. *Adv. Intell. Syst.* **2021**, *3*, 2000099.
(68) Wang, L.; Zheng, C.; Fu, J.; Hua, J.; Chen, J.; Gao, J.; Ling, H.; Xie, L.; Huang, W. Influence of Molecular Weight of Polymer Electret on the Synaptic Organic Field-Effect Transistor Performance. *Adv. Electron. Mater.* **2022**, *8*, 2200155.
(69) Ling, H.; Wang, N.; Yang, A.; Liu, Y.; Song, J.; Yan, F. Dynamically Reconfigurable Short-Term Synapse with Millivolt Stimulus Resolution Based on Organic Electrochemical Transistors. *Adv. Mater. Technol.* **2019**, *4*, 1900471.
(70) Dai, S.; Wu, X.; Liu, D.; Chu, Y.; Wang, K.; Yang, B.; Huang, J. Light-Stimulated Synaptic Devices Utilizing Interfacial Effect of Organic Field-Effect Transistors. *ACS Appl. Mater. Interfaces.* **2018**, *10*, 21472−21480.
(71) Jeong, B. H.; Park, J.; Kim, D.; Lee, J.; Jung, I. H.; Park, H. J. Visible Light-Sensitive Artificial Photonic Synapse. *Adv. Opt. Mater.* **2024**, *12*, 2301652.
(72) Biswas, C.; Güneş, F.; Loc, D. D.; Lim, S. C.; Jeong, M. S.; Pribat, D.; Lee, Y. H. Negative and Positive Persistent Photoconductance in Graphene. *Nano Lett.* **2011**, *11*, 4682−4687.
(73) Liu, K.; Sakurai, M.; Aono, M.; Shen, D. Ultrahigh-Gain Single SnO_2 Microrod Photoconductor on Flexible Substrate with Fast Recovery Speed. *Adv. Funct. Mater.* **2015**, *25*, 3157−3163.
(74) Ji, W.; Zhou, H.; Ye, Y.; Zhao, J.; Xiao, Y.; Lei, S.; Cheng, B. Trap-Related Nonvolatile Negative Photoconductivity in a Single Ag@Al_2O_3 Hybrid Nanorod for a Photomemory with Light-Writing and Bias-Erasing. *Adv. Opt. Mater.* **2019**, *7*, 1901154.
(75) Tan, H.; Liu, G.; Yang, H.; Yi, X.; Pan, L.; Shang, J.; Long, S.; Liu, M.; Wu, Y.; Li, R.-W. Light-Gated Memristor with Integrated Logic and Memory Functions. *ACS Nano* **2017**, *11*, 11298−11305.
(76) Li, N.; He, C.; Wang, Q.; Tang, J.; Zhang, Q.; Shen, C.; Tang, J.; Huang, H.; Wang, S.; Li, J.; et al. Gate-Tunable Large-Scale Flexible Monolayer MoS_2 Devices for Photodetectors and Optoelectronic Synapses. *Nano Res.* **2022**, *15*, 5418−5424.
(77) Lee, M.; Lee, W.; Choi, S.; Jo, J. W.; Kim, J.; Park, S. K.; Kim, Y. H. Brain-Inspired Photonic Neuromorphic Devices Using Photodynamic Amorphous Oxide Semiconductors and their Persistent Photoconductivity. *Adv. Mater.* **2017**, *29*, 1700951.
(78) Ouyang, W.; Teng, F.; He, J. H.; Fang, X. Enhancing the Photoelectric Performance of Photodetectors Based on Metal Oxide Semiconductors by Charge-Carrier Engineering. *Adv. Funct. Mater.* **2019**, *29*, 1807672.
(79) He, H. K.; Yang, R.; Zhou, W.; Huang, H. M.; Xiong, J.; Gan, L.; Zhai, T. Y.; Guo, X. Photonic Potentiation and Electric Habituation in Ultrathin Memristive Synapses Based on Monolayer MoS_2. *Small* **2018**, *14*, 1800079.
(80) Yang, L.; Singh, M.; Shen, S. W.; Chih, K. Y.; Liu, S. W.; Wu, C. I.; Chu, C. W.; Lin, H. W. Transparent and Flexible Inorganic Perovskite Photonic Artificial Synapses with Dual-Mode Operation. *Adv. Funct. Mater.* **2021**, *31*, 2008259.
(81) Zeng, P.; Wang, W.; Han, D.; Zhang, J.; Yu, Z.; He, J.; Zheng, P.; Zheng, H.; Zheng, L.; Su, W.; et al. MoS_2/WSe_2 vdW Heterostructures Decorated with PbS Quantum Dots for the Development of High-Performance Photovoltaic and Broadband Photodiodes. *ACS Nano* **2022**, *16*, 9329−9338.
(82) Kumar, M.; Abbas, S.; Kim, J. All-Oxide-Based Highly Transparent Photonic Synapse for Neuromorphic Computing. *ACS Appl. Mater. Interfaces.* **2018**, *10*, 34370−34376.
(83) Geladi, P.; Manley, M.; Lestander, T. Scatter Plotting in Multivariate Data Analysis. *J. Chemom.* **2003**, *17*, 503−511.

https://doi.org/10.1021/acsnano.4c04851
ACS Nano 2024, 18, 18635−18649

(84) Crow, T. Pavlovian Conditioning of Hermissenda: Current Cellular, Molecular, and Circuit Perspectives. *Learning & Memory* **2004**, *11*, 229−238.
(85) Moon, K.; Park, S.; Jang, J.; Lee, D.; Woo, J.; Cha, E.; Lee, S.; Park, J.; Song, J.; Koo, Y.; Hwang, H. Hardware Implementation of Associative Memory Characteristics with Analogue-Type Resistive-Switching Device. *Nanotechnology* **2014**, *25*, 495204.

https://doi.org/10.1021/acsnano.4c04851
ACS Nano 2024, 18, 18635−18649